Journal Pre-proofs

Room-temperature-stable immunosuppressive nanovesicles for mitigating immunopathology and streamlining cardioprotection post-infarction

Qingsong Tang, Mengting Li, Shengnan Wang, Jingjing Li, Shiyu Cao, Hongman Liu, Yong Wu, Yihuan Chen, Han Shen, Wencheng Zhang, Zhenya Shen, Weiqian Chen

PII: S1385-8947(24)08521-8
DOI: https://doi.org/10.1016/j.cej.2024.157030
Reference: CEJ 157030

To appear in: *Chemical Engineering Journal*

Received Date: 22 July 2024
Revised Date: 26 September 2024
Accepted Date: 21 October 2024

Please cite this article as: Q. Tang, M. Li, S. Wang, J. Li, S. Cao, H. Liu, Y. Wu, Y. Chen, H. Shen, W. Zhang, Z. Shen, W. Chen, Room-temperature-stable immunosuppressive nanovesicles for mitigating immunopathology and streamlining cardioprotection post-infarction, *Chemical Engineering Journal* (2024), doi: https://doi.org/10.1016/j.cej.2024.157030

Room-temperature-stable Immunosuppressive Nanovesicles for Mitigating Immunopathology and Streamlining Cardioprotection Post-infarction

Qingsong Tang[1, #], Mengting Li[1, #], Shengnan Wang[1, #], Jingjing Li[1], Shiyu Cao[1], Hongman Liu[1,3,4], Yong Wu[1], Yihuan Chen[1], Han Shen[1], Wencheng Zhang[2, *], Zhenya Shen[1, *], Weiqian Chen[1, *]

[1] Department of Cardiovascular Surgery of the First Affiliated Hospital & Institute for Cardiovascular Science, Suzhou Medical College, Soochow University, Suzhou, China.

[2] State Key Laboratory for Innovation and Transformation of Luobing Theory; Key Laboratory of Cardiovascular Remodeling and Function Research, Chinese Ministry of Education, Chinese National Health Commission and Chinese Academy of Medical Sciences; Department of Cardiology, Qilu Hospital of Shandong University, Jinan, China

[3] Department of Cardiology, The First Affiliated Hospital of Soochow University, Suzhou, China

[4] Department of Cardiovascular Medicine, the Affiliated Taian City Central Hospital of Qingdao University, Taian, China

[#] These authors contributed equally to this paper

Corresponding authors: Weiqian Chen (chenweiqian@suda.edu.cn), Zhenya Shen (uuzyshen@aliyun.com), and Wencheng Zhang (zhangwencheng@sdu.edu.cn)

Abstract

To understand the role of T lymphocytes during myocardial infarction (MI) progression, public single-cell sequencing data from infarcted murine hearts were re-analyzed, identifying highly heterogeneous T lymphocytes and hyper-activated clusters of proliferative CD8 cytotoxic T lymphocytes. Conventional secretome-based extracellular vesicle therapies often suffer from poor stability and lack of cost-effectiveness. In response, room-temperature-stable, membrane-based nanovesicles enriched with programmed cell death-ligand 1 (PD-L1@NV) have been developed to mitigate T cell-initiated ischemic hyperinflammation. Functionally, PD-L1@NV effectively binds to T cell membranes, suppressing their proliferation and inducing exhaustion in activated CD8 T lymphocytes, thereby supporting myocardial tissue recovery. Mechanistically, PD-L1@NV diminishes CD8 cytotoxic T lymphocyte abundance and augments regulatory T cell population, reshaping *in vivo* T cell dynamics. The development of room-temperature-stable PD-L1@NV presents a straightforward, scalable, and secure strategy for MI treatment, focusing particularly on addressing T cell-driven immunopathology.

Keywords

myocardial infarction; nanovesicle; T lymphocyte; PD-L1; lyophilization

Introduction

Myocardial infarction (MI) stands as a leading cause of morbidity and mortality globally [1]. Timely activation of the immune system in response to myocardial damage is essential for endogenous healing and tissue maintenance [2]. Nevertheless, excessive tissue necrosis may provoke sustained inflammation and disrupt immune self-tolerance, leading to detrimental ventricular remodeling [3, 4]. Clinically, anti-heart autoantibodies to cardiac epitopes have been consistently observed during MI, and the harmful roles of autoreactive T lymphocytes post-MI have been recently established [5]. Notably, CD8 cytotoxic T lymphocytes, a key faction of autoreactive T cells, are mobilized and activated within the ischemic myocardium, where they release inflammatory mediators such as Granzyme B and interferon-γ [6]. Depletion of pathologic CD8 T lymphocytes hampers hyper-inflammatory response, limits myocardial damage, and enhances heart function [6]. These insights highlight the potential of therapeutic interventions targeting pathological CD8 T lymphocytes in MI management.

T lymphocytes exhibit immune checkpoints that interact with inhibitory ligands, crucial for sustaining self-tolerance and averting autoimmunity. Central to this regulatory mechanism is the programmed cell death 1 (PD-1) receptor and its ligand, programmed cell death ligand 1 (PD-L1) [7]. The interaction between PD-1 and PD-L1 induces T-cell exhaustion and dysfunction, thereby mitigating detrimental immunopathology during autoimmunity and infection [8, 9]. It is therefore hypothesized that the introduction of PD-L1 molecule may activate the PD-1/PD-L1 inhibitory axis, consequently mitigating T cell-driven myocardial inflammation.

Cell membrane-based nanovesicle delivery system, renowned for its scalable production and its structural, surficial, and dimensional similarity to conventional cell-free extracellular vesicles [10], holds significant promise for accurate and functional presentation of membranous proteins to specific tissues or cell populations [11, 12]. Despite their pronounced translational potential, most fresh nanovesicle formulations are constrained to short-term applications or necessitate cryopreservation. Lyophilization, also known as freeze-drying, enables the creation of dry nanovesicle formulations, extending their shelf-life and mitigating the need for expensive, labor-intensive cold chain logistics [13]. As basal mesenchymal stem cells (MSCs) express negligible levels of PD-L1 [14], lentivirus-based PD-L1-presenting nanovesicles (PD-L1@NV) were engineered into a room-temperature-stable formulation for MI treatment through serial extrusion and lyophilization. These PD-L1@NVs, by disrupting the PD-1/PD-L1 interaction, suppress the proliferation and activation of CD8 T lymphocytes and mitigate ischemic immunopathology, thereby supporting myocardial tissue repair (Scheme 1). Distinct from traditional secretome-based extracellular vesicle therapies, our extrusion/lyophilization-based membranous nanovesicle approach enhances commercial viability and positions itself as a simple, scalable, stable, and safe therapeutic option for ischemic cardiomyopathy.

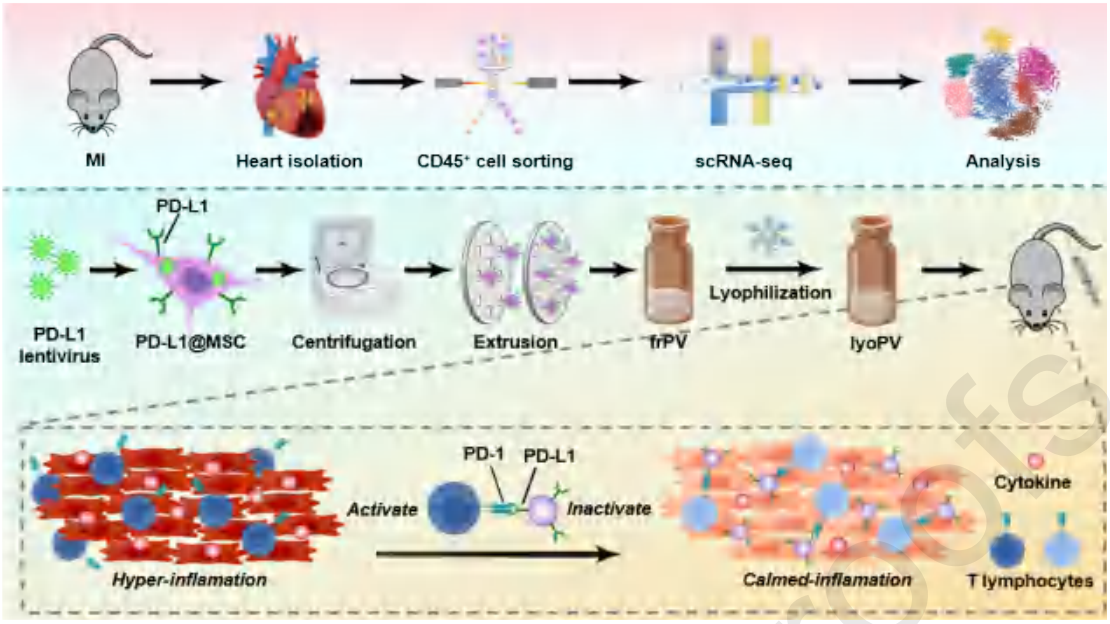

Scheme 1. Schematic model illustrating lyophilized PD-L1@NV mitigates T cell activation, thereby alleviating immunopathology and conferring cardioprotection. Lentivirus-based PD-L1@NVs were engineered into lyophilized formulation via serial extrusion and subsequent lyophilization. By disrupting the PD-1/PD-L1 interaction, these above-mentioned PD-L1@NVs restrain the expansion and activation of CD8 T lymphocytes, alleviating ischemic immunopathology and aiding in myocardial recovery.

Materials and methods

Cell lines

Mesenchymal stem cells derived from the bone marrow of C57BL/6 mice (Cyagen Biosciences) were maintained in DMEM/F12 (6016021, Dakewe) and detached with 0.25% Trypsin-EDTA (TEDTA-10001, Cyagen) [15]. Peripheral blood mononuclear cells (PBMCs), sourced from healthy volunteers with informed consent from all participants, were obtained by Milestone Biological Science & Technology Co., Ltd. Human T lymphoblastoid Jurkat and PBMCs were cultured in RPMI 1640 (6016011, Dakewe) containing 10% FBS (Vivacell) and penicillin/streptomycin (Pricella). For activation, Jurkat cells were exposed to a phorbol-12-myristate-13-acetate (PMA)/ionomycin mixture (CS1001, MultiSciences) for 24 h.

Lentivirus-based gene transduction

Lentivirus encoding membranous murine PD-L1-FLAG and cytosolic EGFP was manufactured by GeneChem, China (GV365). Vector elements were ordered as pUbi-PD-L1-3XFLAG-pCMV-EGFP. Lentivirus-infused supernatant was substituted with fresh DMEM/F12 medium containing 10% FBS (ExCell Bio) 24 h post-infection [16]. Expression and precise localization of target protein were evaluated 72 h post-infection using flow cytometry and immunofluorescence staining.

Preparation of nanovesicles

Cultured cells were thoroughly rinsed to eliminate cellular debris and residual culture medium. The cell suspension was then sonicated in cold PBS containing protease inhibitor (K1007, APExBIO) under a low-power setting (22.5W) for 1 min. The resulting NV was isolated by multistep density gradient ultracentrifugation to exclude nuclear, mitochondrial, lysosomal, and peroxisomal contaminants. To ensure homogeneity, the purified product was subjected to sequential extrusion through a Mini-Extruder (Avanti Polar Lipids) equipped with 400, 200, and 100 nm pore-sized polycarbonate membrane filters [17].

Room-temperature stable formulation

Nanovesicles were converted into dry powder formulation via lyophilization. Briefly, nanovesicles were diluted in PBS containing 25 mM trehalose (PD0021, MultiSciences) at a 1:8 volume ratio of nanovesicle to trehalose-PBS solution. Trehalose functioned as both a cryoprotectant and bulking agent, facilitating adequate powder yield. The diluted NV-trehalose mixture was frozen at -80°C overnight before 24-h lyophilization [18]. All lyophilized powder was maintained at room temperature for subsequent experiments.

Transmission electron microscopy, size distribution, and zeta-potential determination

For morphology, transmission electron microscopy (TEM) was conducted using JEM1400, JEOL, by Wuhan MISP Bio-technology Co., Ltd [19, 20]. For size distribution and zeta potential, dynamic light scattering was performed on Zetasizer Nano ZS (Malvern, ZEN3600).

CFSE Staining and EdU assay

Mouse splenic CD8 cytotoxic T lymphocytes were negatively selected via Mouse CD8 T Cell Isolation Kit (480007, BioLegend). For proliferative CFSE staining [21], mouse CD8 T lymphocytes were labeled with CFSE (5 μM, IC2560, Solarbio) and primed with plate-bound mouse aCD3 (4 μg/mL, clone 17A2, eBioscience) plus mouse aCD28 (4 μg/mL, clone 37.51, Multisciences) for 3 days. Subsequently, indicated nanovesicles (50 μg/mL) were introduced for another 3 days before final detection. For the EdU assay, PBMCs were similarly primed with plate-bound human aCD3 (10 μg/mL, clone OKT3, Invitrogen) plus aCD28 (4 μg/mL, clone CD28.2, MultiSciences) for 3 days and then treated with indicated interventions for additional 2 days. EdU assay (C0081S, Beyotime) was performed on Day 5 [22]. Briefly, cells were incubated with 10 μM EdU for 6 h, and nuclear EdU was detected by attachment of AF647-labeled azide to its alkyne group. Both CFSE tracing and EdU incorporation were analyzed via flow cytometry (Millipore Guava easyCyte).

ELISPOT assay

The proportion of IFN-γ-secreting CD8 T lymphocytes was quantified using ELISPOT assay (2210002, Dakewe) [23]. Briefly, aCD3/28-activated CD8 T lymphocytes were incubated with indicated nanovesicles (50 μg/mL) and transferred into IFN-γ capture antibody pre-coated ELISPOT wells (10^5 per well). IFN-γ-secreting spot-forming units were analyzed using IRIS FluoroSpot/ELISPOT reader (Mabtech) for multiplexing at the single-cell level.

Single-cell sequencing dataset analysis

The single-cell dataset for MI was obtained from the GEO database (Accession number: GSE163465). Low-quality cells were filtered out, and data from different samples were integrated using Seurat (version 5.1.0) [24]. The dimensional reduction was performed using RunPCA and RunUMAP, followed by clustering with FindNeighbors and FindClusters. Differential cell markers were identified using the FindAllMarkers function, and plots were generated with ggplot2 (version 3.5.1). Cell annotation was carried out via PanglaoDB (https://panglaodb.se/search.html) [25], with T lymphocytes further re-clustered using the Seurat pipeline. FindMarkers identified differentially expressed genes between MI samples (Days 3, 7, and 14 post-MI) and sham controls, and these were visualized in a volcano plot using ggplot2. Genes with log2 fold change (log2FC) > 1 and adjusted P-value < 0.05 were classified as differentially expressed genes. Functional enrichment analysis was performed with the Metascape database (https://metascape.org) [26] and GSEA analysis was conducted using the clusterProfiler package (version 4.8.3) [27].

RNA sequencing and genome-wide transcriptome analysis

For RNA-seq analysis, aCD3/28-activated mouse CD8 T lymphocytes underwent various interventions for two days, followed by total RNA extraction and mRNA enrichment, fragmentation and reverse transcription. These resulting cDNA fragments were then end-repaired, base-added, and ligated for amplification. The cDNA library was sequenced on the Illumina Novaseq 6000 platform (Gene Denovo Biotechnology) [28, 29]. Differentially expressed genes were defined as false discovery rate < 0.05 and absolute fold change > 1.5. Data analysis was conducted using Omicsmart (http://www.omicsmart.com).

PD-L1@NV biodistribution

PD-L1@NVs were labeled with DiR (22070, AAT Bioquest) in saline. Following incubation at 37 °C for 2 h, DiR-labeled PD-L1@NVs were washed with saline three times. The MI mice were injected with 200 μg DiR-labeled PD-L1@NV via the tail vein (1 μg/μL, protein weight). Accumulation of PD-L1@NVs in the heart and other major organs was observed through an in vivo imaging system (PerkinElmer) [30, 31].

Animals and treatments

Animal protocols were approved by the Animal Care and Use Committee of Soochow University (SUDA20231219A01) and conducted under the Ministry of Health, China's Guide for the Care and Use of Laboratory Animals. NV or PD-L1@NV (100 μg/mouse/injection) were administered intravenously via the tail vein. Concurrently, for PD-L1 blockade, aPD-L1 (20 μg/mouse/injection, A2115, Selleck) and for CD8 T cell depletion, aCD8a (75 μg/mouse/injection, A2102, Selleck) were similarly delivered through intravenous tail vein injections.

Mouse MI model and cardiac functional assessment

MI was conducted on male C57BL/6 mice [32, 33]. Briefly, a permanent ligation was induced on the left anterior descending artery through a left thoracotomy. Cardiac ischemia was evidenced by visible myocardial blanching or cyanosis and swelling of the left atrium. Subsequently, the chest cavity was meticulously closed to re-establish negative pressure and prevent pneumothorax.

Cardiac systolic function was monitored by echocardiography employing the Vevo 2100 system (VisualSonics) fixed with a 30-MHz transducer [34, 35]. M-mode ultrasound imaging was utilized to measure the contraction and relaxation phases of the hearts, enabling precise measurement of both ejection fraction and fractional shortening.

Tissue digestion and flow cytometry

Infarcted myocardium was quickly excised, finely minced, and subjected to enzymatic digestion in 2% Type II Collagenase (BS164, Biosharp), 0.25% elastase (Worthington), and 0.05% DNase I (Solarbio) as previously described [36]. For flow cytometry of splenocytes, dissected spleens were ground mechanically to achieve a smooth consistency. All dissociated cells underwent red blood cell lysis before flow cytometry.

To enrich NVs, aldehyde/sulfate latex beads (4 μm) were used before antibody staining [37]. Both cultured and isolated cells were stained with a panel of fluorescently conjugated antibodies along with corresponding isotype controls (Elabscience) [38, 39]. After immunostaining, these cells were analyzed using a Millipore Guava easyCyte flow cytometer. CD8 and CD4 T lymphocytes were identified as $CD8^+CD3^+$ and $CD4^+CD3^+$, respectively. Antibody details are shown in Table S1 (Supporting Information).

Masson's trichrome and H&E staining

For heart cross-sections, infarcted hearts were arrested in 10% KCl, fixed with 4% paraformaldehyde (M40958, AbMole), and cut into 5-μm slides. Infarct percentage was visualized using Masson's trichrome staining and quantified as the ratio of scar area to the sectional area [40-42]. For morphological assessment of major organs, the brain, spleen, kidney, lung, and liver were paraffined-embed and H&E-stained (KeyGEN BioTECH) [43, 44].

In vivo **safety evaluation**

Serum levels of aspartate aminotransferase (AST, BC1565, Solarbio), alanine aminotransferase (ALT, BC1555, Solarbio), blood urea nitrogen (BUN, BC1535, Solarbio), and creatinine (CRE, C011-2-1, Nanjing Jiancheng) were quantified using their respective assay kits [45, 46].

Tissue immunohistochemistry staining and immunofluorescence staining

For immunohistochemistry, formalin-fixed sections were subjected to rehydration and EDTA-induced epitope retrieval, followed by sequential incubation with anti-PD-1 and HRP-conjugated secondary antibodies [47]. The slides were finally incubated with DAB substrate for observable brown coloration. Nuclei were counterstained with hematoxylin.

For membranous labeling, Griffonia (Bandeiraea) simplicifolia lectin 1 (1 mg/mL, L-1100, Vector) was added into the culture medium 15 min before fixation. For immunofluorescence staining, adherent cells were fixed, permeabilized, and sequentially stained with primary and fluorescent-conjugated secondary antibodies (Yeasen) [48, 49]. For nuclear visualization, cells were counterstained with DAPI Fluoromount-G anti-fade solution (36308ES20, Yeasen) [50]. Visualization was performed using an inverted confocal microscope (Zeiss, LSM880). Antibody

details are shown in Table S1 (Supporting Information).

Western blot

Nanovesicles were lysed with RIPA lysis buffer (K1120, APExBIO, Houston, USA) supplemented with PMSF and InStab Protease Inhibitor Cocktail (20124ES03, Yeasen). Protein samples were loaded with 5×Protein SDS PAGE Loading Buffer (PM099, Novoprotein) and separated on FuturePAGE 4-20% SDS-PAGE gels (ET12420Gel, ACE) and transferred into PVDF membranes via NcmBlot Rapid Transfer Buffer (WB4600, New Cell & Molecular Biotech). After incubation via BSA Blocking Buffer (CW0054, CoWin) and specific antibodies, visualization was achieved through ECL Detection Kit (KGC4601-100, KeyGEN BioTECH) [42, 51]. For re-probing, membranes were stripped using Western Blot Fast Stripping Buffer (PS107S, EpiZyme). Antibody details are shown in Table S1 (Supporting Information).

Quantitative real-time PCR

mRNA levels were quantified using quantitative real-time PCR [50, 52]. Briefly, RNAs were extracted via RaPure Total RNA Micro Kit (R4012, Magen) and their concentration was determined with a NanoDrop spectrophotometer. Complementary cDNA synthesis was conducted via HiScript IV RT SuperMix for qPCR (+gDNA wiper) (R423-01, Vazyme). Quantitative real-time PCR was performed with a WitEnzy 2× SYBR Green qPCR Master Mix (8073021, Dakewe). The relative mRNA expression was calculated as $2^{-(\triangle\triangle CT)}$ and normalized to 18S. Primers for PD-1 and 18S were synthesized by GENEWIZ. Primer details are shown in Table S2 (Supporting Information).

Statistical analysis

All data were presented as mean ± SEM and were processed using GraphPad Prism. Comparisons between two groups were performed using a two-tailed unpaired Student's *t*-test, while those involving more than two groups utilized either one-way or two-way ANOVA with Tukey correction. *: $P < 0.05$ was defined as statistically significant.

Results and discussion

T lymphocyte activation is enhanced during myocardial infarction progression

To explore the function of T lymphocytes during MI progression, we re-analyzed single-cell sequencing data from infarcted murine hearts (GSE163465), identifying nine distinct $CD45^+$ immune cell clusters (Figure 1A). On Day 7 post-MI, notable shifts in the distribution of these clusters were apparent, with a significant increase in T lymphocytes (Figure 1B). All T lymphocytes were further categorized into six subsets: CD8 T, memory T, activated CD4, Th17, natural killer T (NKT), and regulatory T (Tregs) (Figure 1C). Particularly, CD8 T lymphocytes, known for their cytotoxic capabilities, exhibited a marked expansion since Day 3 and remained elevated through Day 14 post-MI (Figure 1D), with a unique transcriptional profile and specified functions (Figure f1E). We pooled data from CD8 T lymphocytes on Days 3, 7, and 14 post-MI into a single dataset and specifically identified significant upregulation of genes such as Lymphocyte Antigen 6 Family Member D (*Ly6d*) and Perforin 1 (*Prf1*) (Figure 1F). Notably, *Ly6d* is expressed in common lymphoid progenitors and modulates lymphocyte specification [53], while *Prf1* encodes perforin, a CD8 T lymphocyte-released pore-forming protein that elevates membrane permeability and aggravates inflammatory cell infiltration and cytokine release [54]. Consistently, gene ontology (GO) enrichment analysis of differentially expressed genes highlighted their novel participation in cell cycle and proliferation (Figure 1G). Finally, CD8 T lymphocytes in ischemic myocardium exhibited upregulated expression of genes linked to Interleukin-1 beta production, chemokine-mediated signaling, and lymphocyte migration (Figure 1H-J), suggesting intensified activation and clustering in the infarct zone. These findings imply substantial proliferation and activation of CD8 T lymphocytes post-MI, potentially contributing to a prolonged hyper-inflammatory response.

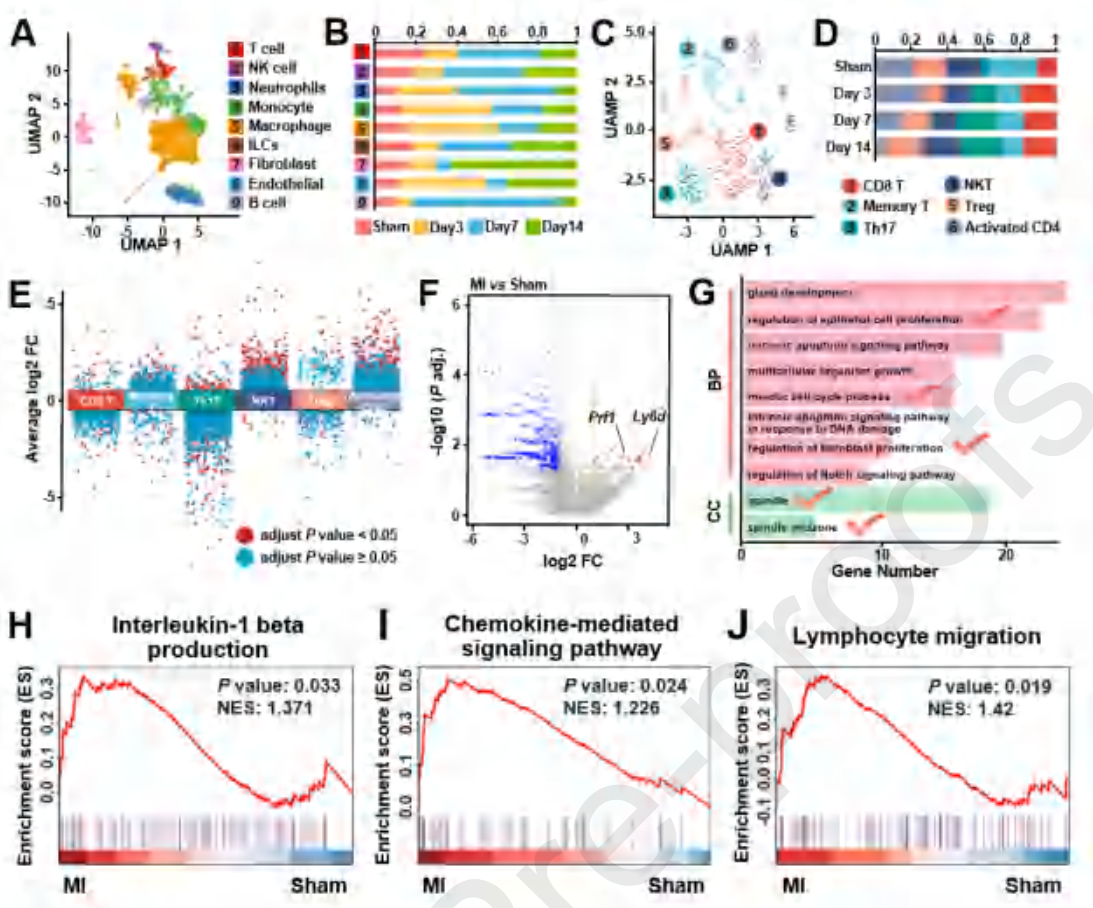

Figure 1. T lymphocytes were highly heterogeneous and robustly activated throughout MI progression. (A) UMAP visualization of cardiac CD45^{+} immune cells pooled from MI and Sham groups, categorized by canonical marker genes. (B) Relative ratio of each immune cell type within all cardiac immune cells during MI progression. (C) UMAP plot of subclustered T lymphocytes color-coded by major cell lineages. (D) Proportion of each T lymphocyte subsets relative to all cardiac T lymphocytes during MI progression. (E) Differential gene expression analysis unveiling up- and down-regulated genes across all six T lymphocyte subsets, with adjusted *P*-values < 0.05 in red and $\geqslant$ 0.05 in blue. (F-J) All CD8 T lymphocytes from different post-MI time points were pooled into a single dataset and subjected to differential gene analysis with the Sham group. Volcano plot (F) and gene ontology enrichment terms (G) for CD8 T lymphocyte between MI and Sham groups. (H-I) Gene set enrichment analysis focusing on gene sets involved in Interleukin-1 beta production, chemokine-mediated signaling pathway, and lymphocyte migration. The *P*-values and Normalized Enrichment Scores (NES) were shown in each pathway.

PD-L1@NV is room-temperature stable in dry powder formulation

To fabricate the immunomodulatory PD-L1@NV, we first established a lentivirus-based PD-L1@MSC cell line using conventional murine bone-marrow-derived mesenchymal stem cells (Figure S1, Supporting Information). This cell line displayed the presence of both membranous PD-L1-FLAG fusion protein and intracellular EGFP protein (Figure 2A). Morphologically, PD-L1@MSC displayed either spindle-shaped or irregular triangular forms, alongside abundant cytosolic EGFP signals (Figure S2A, Supporting Information), reflecting effective lentiviral transduction. Consistently, flow cytometry further confirmed a substantial 299.8-fold elevation in PD-L1 expression within PD-L1@MSC (Figure S2B, Supporting Information), affirming successful gene delivery. Finally, confocal imaging verified the co-localization of PD-L1 and FLAG with membrane-bound lectin (Figure 2B; Figure S2C, Supporting Information), ensuring precise protein targeting to the cell membrane. In summary, these results delineated the intentional overexpression and accurate membranous localization of PD-L1-FLAG in PD-L1@MSC.

To generate nano-scale interventions, PD-L1@MSC was subjected to sonication to isolate its membranous fraction, which was then purified through multistep density gradient ultracentrifugation to remove nuclear, mitochondrial, lysosomal, and peroxisomal fractions. To achieve uniform size distribution, fresh PD-L1@NV (frPV) was produced via serial extrusion through nanoscale pore-sized membrane filters. To facilitate easier storage and administration, we converted our liquid PD-L1@NV into dry powder formulation, termed lyophilized PD-L1@NV (lyoPV), and its physicochemical properties were assessed post-reconstitution (Figure 2C). To ascertain the stability of these lyophilized PD-L1@NV following room-temperature storage, morphology was compared among different formulations. Transmission electron microscopy (TEM) revealed that all NVs maintained their round shape and membranous structure. Crucially, lyophilization and subsequent rehydration processes preserved their membrane integrity (Figure 2D&E). Further characterization by dynamic light scattering indicated an average diameter of about 150 nm (Figure 2F) and an average zeta potential of approximately -30 mV for all formulations (Figure 2G), indicating uniform vesicle size and charge. Notably, all NV formulations were verified to express exclusively membranous Na^+-K^+ ATPase, with negligible cytosolic GAPDH or nuclear Histone H3 contamination (Figure 2H). Finally, both western blot and latex bead-based flow cytometry demonstrated comparably high levels of FLAG (Figure 2H) and PD-L1 (Figure 2I-K) in both fresh and lyophilized PD-L1@NV, suggesting that the lyophilized formulation retains its immune-regulatory efficacy. Collectively, these findings confirmed the successful preparation of PD-L1@NV, with the lyophilized variant exhibiting noteworthy stability at room temperature.

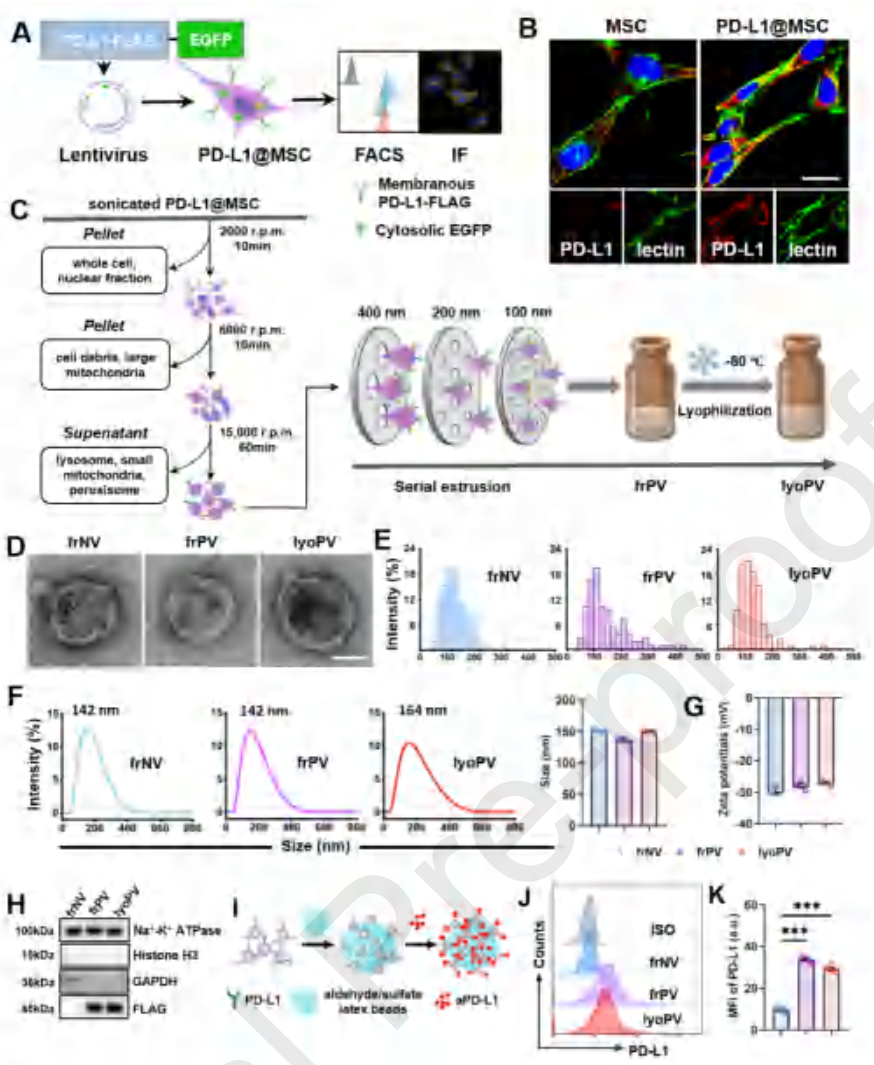

Figure 2. Generation and characterization of lyophilized PD-L1@NV. (A) Diagram depicting the creation of lentivirus-based PD-L1@MSC, showcasing membranous PD-L1-FLAG and intracellular EGFP. (B) Colocalization of PD-L1 with membrane-bound lectin by immunofluorescence. Scale bar, 20 μm. (C) Schematic diagram detailing the production of fresh and lyophilized PD-L1@NV. (D) Characteristic TEM images of fresh NV (frNV), fresh PD-L1@NV (frPV), and lyophilized PD-L1@NV (lyoPV). Scale bar, 50 nm. (E) Size distribution measured from TEM images. (F&G) Size distribution and zeta potential measured via dynamic light scattering (n = 3). (H) Western blot analyses of membranous Na^+-K^+ ATPase, nuclear Histone H3, cytosolic GAPDH, and FLAG. (I-K) Flow cytometry histogram plots for membranous PD-L1, pre-captured on aldehyde/sulfate latex beads (n = 6). Values were expressed as mean ± SEM and calculated via one-way ANOVA with Tukey correction. ***: $P < 0.001$.

Targeted binding and complicated modulation of CD8 T lymphocytes by PD-L1@NV

Considering the interaction between the PD-1 receptor and its ligand PD-L1, we investigated the physical binding and functional modulation of PD-L1@NV on CD8 T lymphocytes. Firstly, it is worth noting that there was a notable elevation in PD-1 mRNA level within PMA/ionomycin-activated T lymphoblastoid Jurkat cells (Figure 3A). Consequently, both fresh and lyophilized PD-L1@NV

exhibited significant co-localization with membranes of activated Jurkat cells (Figure 3B). To unbiasedly elucidate its cellular functions, RNA-seq analysis was performed on PD-L1@NV-treated CD8 T lymphocytes (Figure 3C). Among 1032 differentially expressed genes, 123 were downregulated and 909 were upregulated (Figure 3D), with notable enrichment in pathways related to “immune system”, “replication and repair”, and “cell growth and death” (Figure 3E). Specifically, the molecular signature of these lymphocytes was characterized by the top 10 enriched GO terms, all strongly associated with cell cycle regulation (Figure 3F). Finally, gene set enrichment analysis (GSEA), which facilitates biological interpretation via effectively identifying concordant differences at the gene set level [55], was conducted to identify dysregulated pathways following PD-L1@NV therapy. Notably, an upregulation of the “negative regulation of cell cycle” pathway was observed (Figure 3G), indicating weakened cell proliferation. Additionally, upregulation of the “negative regulation of lymphocyte activation” pathway, along with downregulation of the “oxidative phosphorylation” pathway (Figure 3H&I) suggested diminished activation of CD8 T lymphocytes. Collectively, these findings implied that PD-L1@NV robustly binds to CD8 T lymphocytes, exerting complicated immunological functions.

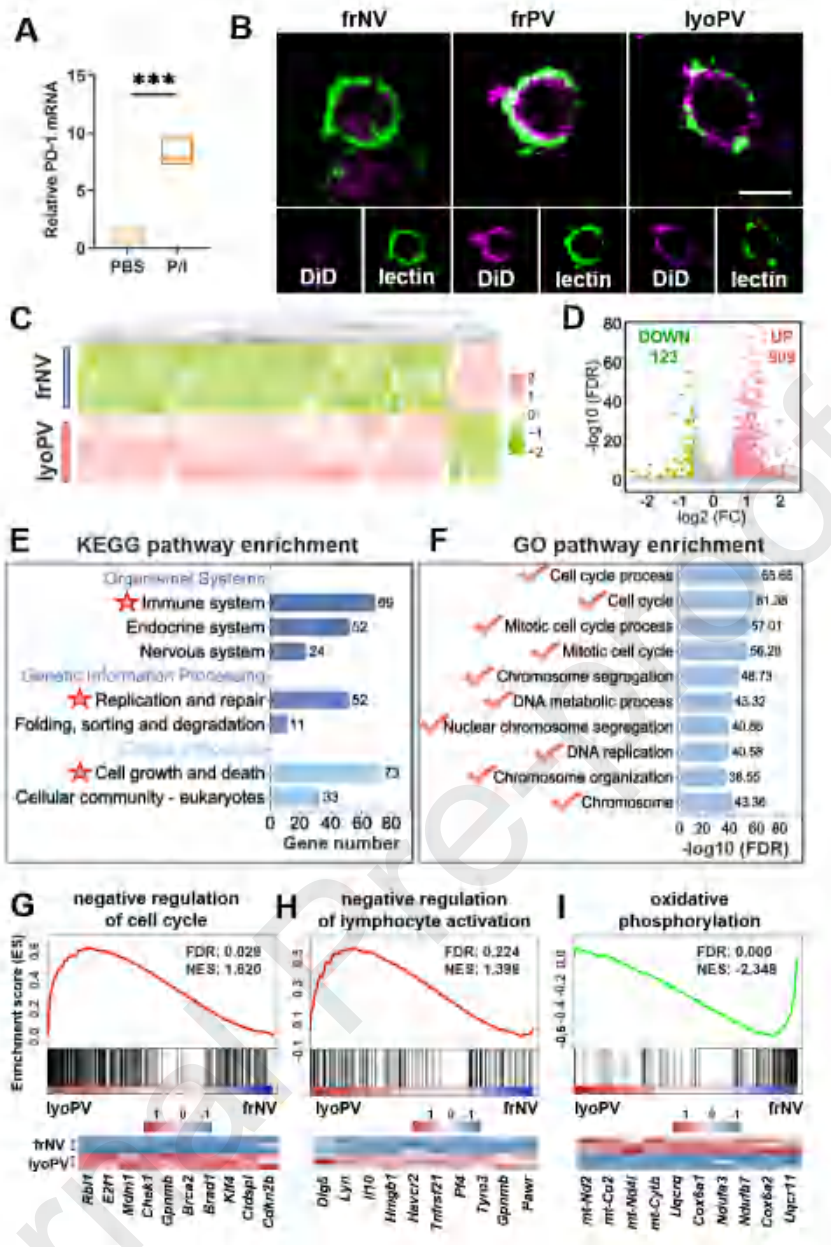

Figure 3. Targeted binding and intricate cellular functions by PD-L1@NV. (A) PD-1 mRNA expression in PMA/ionomycin (P/I)-primed Jurkat cells (*n* = 4). (B) Co-localization of DiD-labeled PD-L1@NV with membranous lectin in P/I-primed Jurkat cells. Scale bar, 5 μm. (C-I) mouse aCD3/CD28-activated CD8 T lymphocytes were incubated with specified interventions and subjected to RNA sequencing (*n* = 3). (C&D) Heatmap and volcano plot illustrating differential gene expression. (E&F) Analyses of significantly differential genes via the Kyoto Encyclopedia of Genes and Genomes (KEGG) and Gene Ontology (GO), with GO terms ranked by their significance (Benjamini-Hochberg corrected p-value). (G-I) Enrichment plots (upper) and cutting-edge gene expression heatmaps (lower) for key dysregulated pathways in CD8 T lymphocytes. FDR, false discovery rate; NES, normalized enrichment score. Values were expressed as mean ± SEM and calculated via unpaired Student's *t*-test. **: $P < 0.01$.

PD-L1@NV restrains proliferation and activation of CD8 T lymphocytes

To further delineate the modulatory effects of PD-L1@NV on cell cycle, a CFSE dilution assay was performed on CD8 T lymphocytes. Briefly, mouse CD8 T lymphocytes (Figure S3A&B, Supporting Information) were CFSE-labeled, aCD3/28-activated, and exposed to indicated interventions (Figure 4A). Importantly, both fresh and lyophilized PD-L1@NVs exhibited marked but comparative suppression against CD8 T proliferation (Figure 4B), a finding corroborated by EdU incorporation assay in human peripheral blood mononuclear cells (Figure 4C&D). Additionally, the immunomodulatory ability of PD-L1@NV on cellular activation and cytokine production in mouse CD8 T lymphocytes was assessed through ELISPOT-based IFN-γ release. Importantly, both fresh and lyophilized PD-L1@NV induced comparable IFN-γ-secreting spot forming, much less than those produced by NV control (Figure 4E&F), indicating activity blockage by PD-L1@NV. In sum, these findings supported the hypothesis that PD-L1@NV exerts a suppressive role in the proliferation and activation of CD8 cytotoxic T lymphocytes, thereby potentially calming the ischemic hyper-inflammatory milieu.

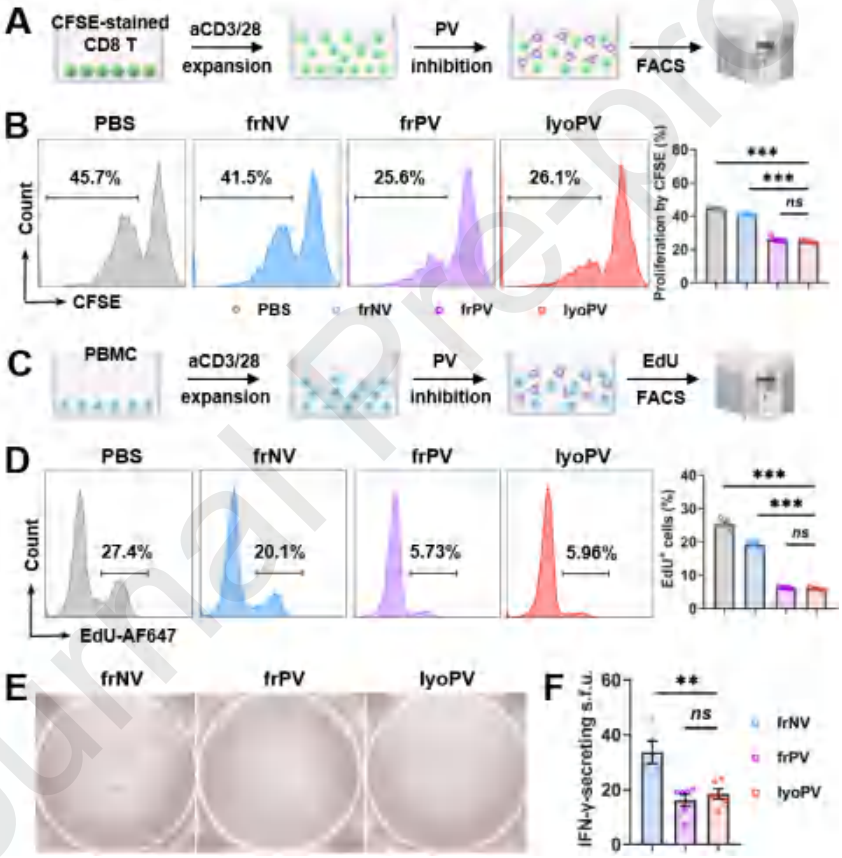

Figure 4. Suppressive effects of PD-L1@NV on CD8 T lymphocyte proliferation and activation. (A&B) CD8 T lymphocyte-based CFSE assay. Mouse splenic CD8 T lymphocytes were treated with plate-bound aCD3/CD28 and designated PD-L1@NV before proliferative CFSE assay. (A) Schematic illustration. (B) Flow cytometry histogram plots and quantification (n = 4). (C&D) PBMC-based EdU assay. PBMCs were stimulated with plate-bound aCD3/CD28 and specified PD-L1@NV before proliferative EdU assay. (C) Schematic diagram. (D) Flow cytometry histogram plots and quantification (n = 5). (E) ELISPOT assay evaluating IFN-γ-releasing spots by aCD3/28-activated CD8 T lymphocytes. (F) Quantified IFN-γ-secreting spot forming per 10^5 cells (n = 6). s.f.u., spot-forming units. Values were expressed as mean ± SEM and calculated via unpaired

Student's *t*-test or one-way ANOVA with Tukey correction, as appropriate. ***: $P < 0.001$, **: $P < 0.01$, *ns*: not significant.

In vivo biodistribution of PD-L1@NV

To explore the therapeutic potential of PD-L1@NV in MI treatment, we explored its biodistribution *in vivo*. Firstly, immunohistochemistry demonstrated a 7.50-fold higher PD-1 protein level in infarcted compared with healthy myocardium ($P < 0.001$, Figure 5A&B). Furthermore, in the setting of ischemic hearts, PD-1 expression also seemed to be 1.99-fold upregulated in ischemic compared to the remote zone ($P < 0.05$, Figure 5C&D). In line with these findings, *ex vivo* imaging unveiled greater myocardial (9.37 ± 0.66 *vs*. 7.25 ± 0.63, $P < 0.05$) but less hepatic retention (96.21 ± 3.31 *vs*. 116.0 ± 7.05, $P < 0.05$) of DiR-labeled PD-L1@NV in MI mice (Figure 5E). Finally, compared to other major organs such as the liver and kidney, the ischemic heart exhibited significant PD-L1@NV accumulation (6.38 ± 0.57 vs. 4.01 ± 0.09, P < 0.01; Figure S4, Supporting Information).

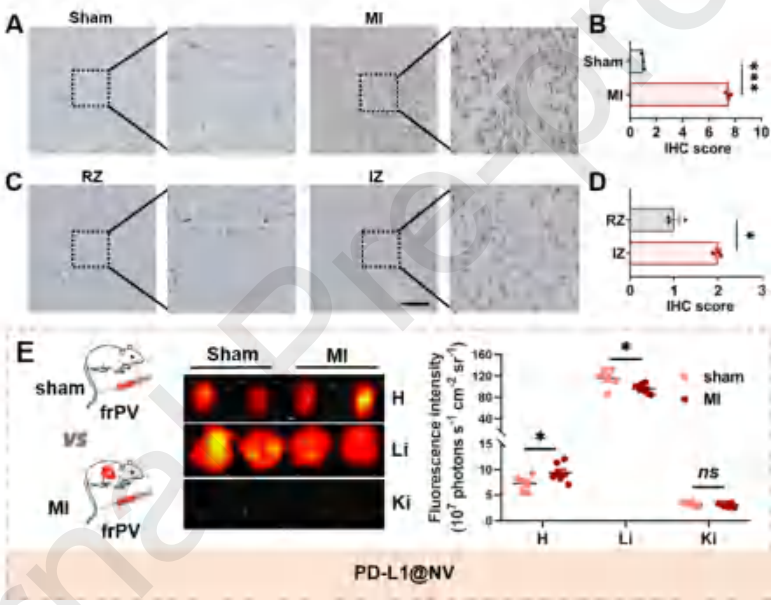

Figure 5. Biodistribution of immunosuppressive PD-L1@NV *in vivo*. (A&B) Immunohistochemistry of PD-1 expression in healthy (sham) and MI mice ($n = 3$). Scale bar, 100 μm. (C&D) Immunohistochemistry of PD-1 expression in the ischemic zone (IZ) compared with the remote zone (RZ) of MI mice ($n = 3$). Scale bar, 100 μm. (E) DiR-labeled PD-L1@NV was injected via the tail vein of healthy and MI mice and *ex vivo* optical imaging of major organs was shown ($n = 6$ for sham, $n = 7$ for MI). H, heart; Li, liver; Ki, kidney. Values were expressed as mean ± SEM and calculated via unpaired Student's *t*-test or one-way ANOVA with Tukey correction, as appropriate. ***: $P < 0.001$, *: $P < 0.05$, *ns*: not significant.

Room-temperature stable PD-L1@NV significantly improves cardiac function in MI mice

Motivated by the promising *ex vitro* evidence that lyophilized PD-L1@NV curtailed proliferation and activation of CD8 T lymphocytes, we explored its cardioprotective effects on MI mice (Figure 6A). Specifically, cardiac function was quantitatively assessed by measuring left ventricular

ejection fraction (EF) and fractional shortening (FS) and PD-L1@NV therapy significantly improved EF compared to the NV control on Day 28 post-MI (Figure 6B&C), reflecting considerable improvements in cardiac function. This marked enhancement was also mirrored in FS metrics (Figure 6D). Notably, PD-L1@NV effectively facilitated structural recovery, as evidenced by reduced heart weight (Figure 6E) and scar area (Figure 6F). Further validation came from Masson trichrome staining, which highlighted pronounced myocardial preservation and greater amounts of viable heart tissue after PD-L1@NV therapy (Figure 6G&H). Interestingly, all these therapeutic benefits appeared reversible upon additional challenge with PD-L1-neutralizing antibody (aPD-L1) (Figure 6B-H), confirming dependency on the PD-1/PD-L1 inhibitory axis. Overall, these results suggested that PD-L1@NV significantly enhances cardiac function and aids in post-MI ischemic repair, mediated through its enriched PD-L1 molecule.

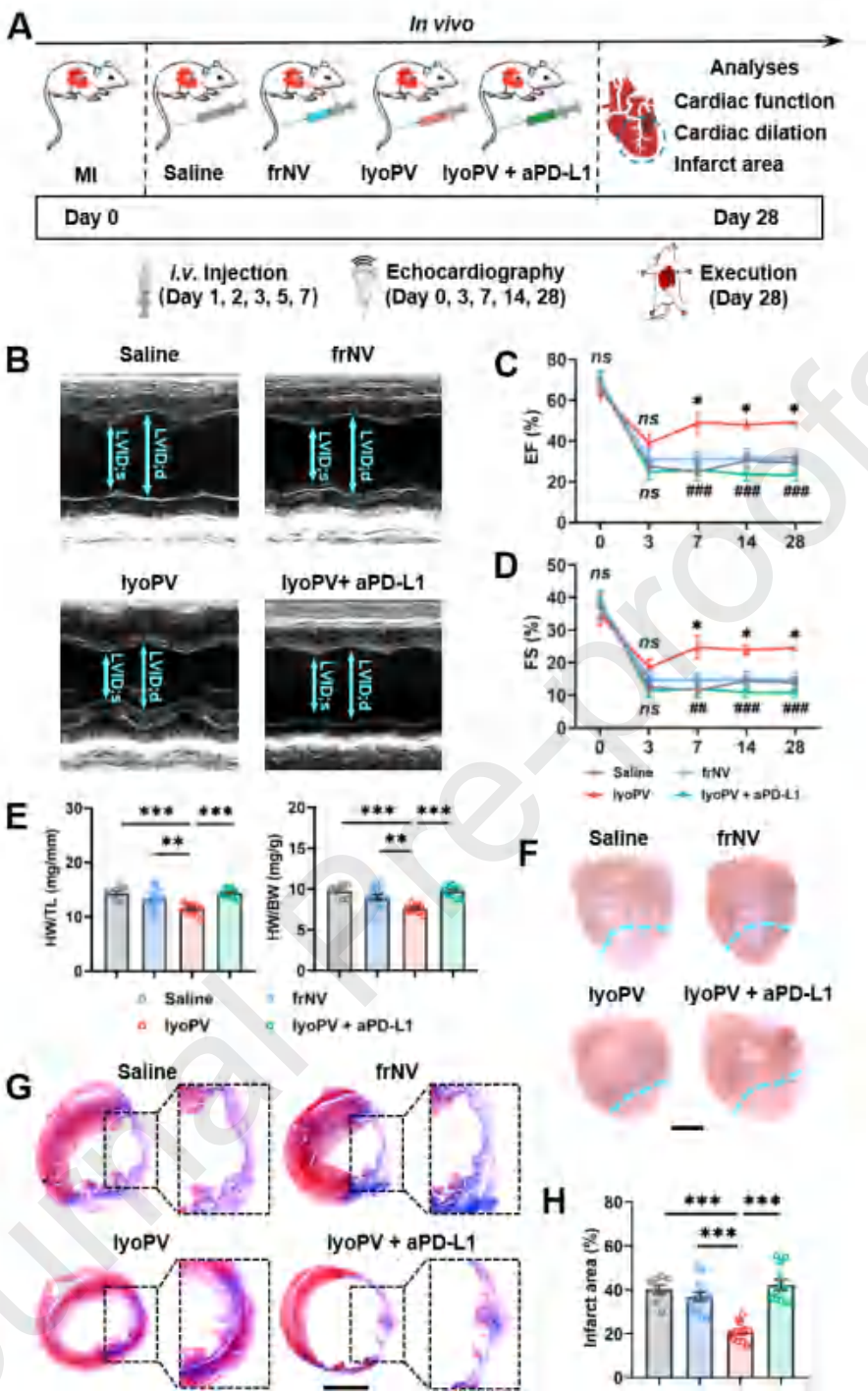

Figure 6. Cardioprotective effects of engineered PD-L1@NV *in vivo*. (A) Experimental pipeline for cardioprotection evaluation of engineered PD-L1@NV. (B) Characteristic M-mode images obtained on Day 28 post-MI. (C&D) Ejection fraction (EF%) and fractional shortening (FS%) standing for heart function were presented as time curves (n = 7 for Saline, frNV, and lyoPV; n = 8 for lyoPV + aPD-L1). * for comparison between PD-L1@NV and NV, # for comparison between PD-L1@NV and PD-L1@NV + aPD-L1) (E) Quantification of heart weight normalized to tibia length or body weight. (F) Characteristic heart images on Day 28 post-MI, with infarct area indicated by blue lines. Scale bar, 2 mm. (G&H) Masson trichrome staining on Day 28 post-MI, along with the percentage of infarct area. Scale bar, 2 mm. Values were expressed as mean ±

SEM and calculated via one-way or two-way ANOVA with Tukey correction, as appropriate. ***/###: $P < 0.001$, **: $P < 0.01$, */#: $P < 0.05$, *ns*: not significant.

Immunomodulatory effects of PD-L1@NV on T cell dynamics

Following MI, CD8 T lymphocytes are recruited to the ischemic heart, exacerbating immunopathology and thereby impairing myocardial function [56]. Inspired by the *ex vitro* suppression of CD8 T lymphocytes and cardioprotective properties of lyophilized PD-L1@NV, we evaluated *in vivo* T cell dynamics post-therapy (Figure 7A). Notably, PD-L1@NV therapy significantly reduced the frequency of $CD8^+CD3^+$ cytotoxic T lymphocytes in both the heart and spleen (Figure 7B&C). Additionally, compromised functionality of T cells was evidenced by diminished splenic IFN-γ- and Granzyme B-producing cells (Figure S5A-D, Supporting Information), alongside their corresponding mRNAs in ischemic heart (Figure S5E&F, Supporting Information). Specifically, the proportion of splenic $CD4^+CD3^+$ helper T lymphocytes similarly exhibited substantial immunosuppression, with PD-L1@NV-treated mice showing the lowest percentage (Figure 7D). In contrast, an increase in $CD25^+CD4^+CD3^+$ regulatory T lymphocytes, a potent inflammatory response suppressor, was observed following PD-L1@NV therapy (Figure 7E). This finding is supported by literature indicating that Treg depletion exacerbates left ventricular dilation, whereas their expansion mitigates myocardial inflammation and leukocyte infiltration [57]. Importantly, all these effects were reversible by aPD-L1 intervention (Figure 7B-E; Figure S5A&B, Supporting Information), confirming the involvement of PD-L1. In summary, these results suggested that PD-L1@NV effectively modulates T cell population and functionality, fostering an immunosuppressive milieu that promotes MI recovery.

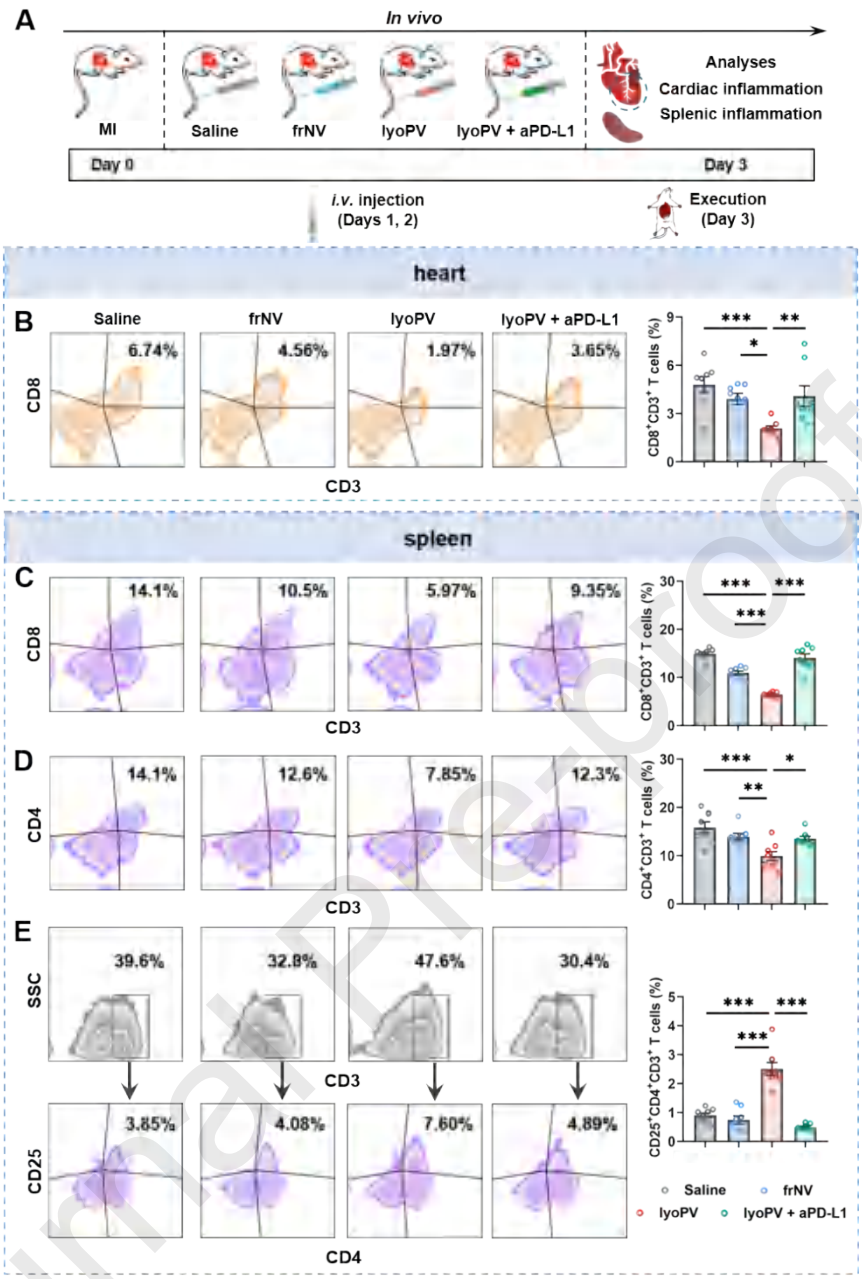

Figure 7. Blunted post-MI T cell profiling by immunosuppressive PD-L1@NV. (A) Experimental outline for T cell activation by engineered PD-L1@NV. (B&C) Flow cytometry zebra plots analyzing CD8 cytotoxic T lymphocytes ($CD8^+CD3^+$) from the heart and spleen (n = 8). (D) Flow cytometry zebra plots demonstrating splenic CD4 helper T lymphocytes ($CD4^+CD3^+$) along with quantitative analysis (n = 8). (E) Flow cytometry zebra plots for splenic $CD25^+CD4^+CD3^+$ Treg lymphocytes accompanied by quantitative analysis (n = 8). Values were expressed as mean ± SEM and calculated via one-way ANOVA with Tukey correction. ***: $P < 0.001$, **: $P < 0.01$, *: $P < 0.05$.

Cardioprotective mechanism of PD-L1@NV through modulation of CD8 T lymphocytes

To elucidate the cardioprotective mechanism of PD-L1@NV, particularly its potential modulation on CD8 T lymphocytes, we employed CD8-neutralizing antibody (aCD8) to deplete these cells

(Figure S6A, Supporting Information). The efficacy of aCD8 in clearing CD8 T lymphocytes from the heart, spleen, and peripheral blood was quantified, revealing significant reductions of 56.34%, 97.76%, and 96.58% in these tissues, respectively (Figure S6B, Supporting Information). Following the removal of CD8 T lymphocytes, PD-L1@NV was administered to MI mice at defined intervals, with subsequent assessments of cardiac function and pathology (Figure 8A). Specifically, echocardiography on Day 28 highlighted notable cardioprotection in the PD-L1@NV-treated group; yet this effect was markedly diminished by aCD8 administration (Figure 8B-D). This reduction in cardioprotection was further supported by an elevation in infarct size and relative heart weight in PD-L1@NV plus aCD8 group (Figure 8E&F), indicative of pathological hypertrophy. Finally, Masson trichrome staining highlighted an exacerbated scar area after CD8 T lymphocyte exhaustion (29.70 ± 2.48% *vs*. 20.40 ± 1.53%, Figure 8G&H). In conclusion, our data compellingly indicated that the cardioprotective efficacy of PD-L1@NV is fundamentally linked to its suppression of CD8 cytotoxic T lymphocytes.

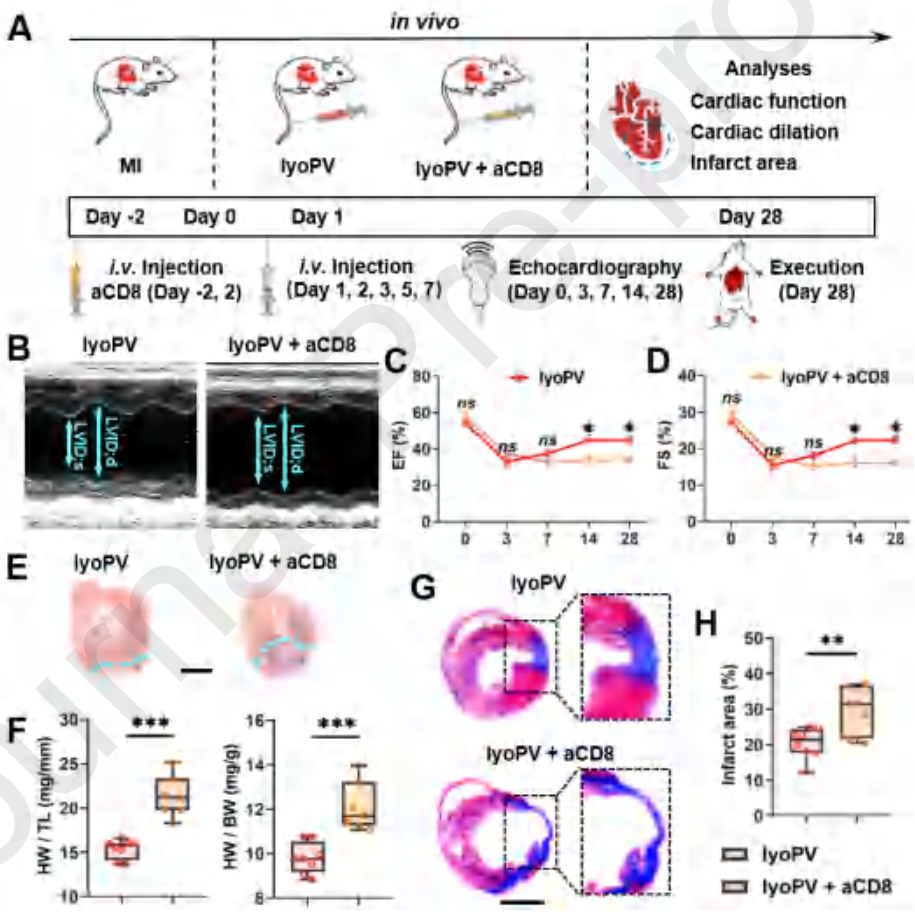

Figure 8. Elimination of CD8 T lymphocytes dramatically attenuated the cardioprotective effects of PD-L1@NV. (A) Experimental framework for the cardioprotective effect of lyophilized PD-L1@NV after clearance of CD8 cytotoxic T lymphocytes. (B) Characteristic M-mode images obtained on Day 28 post-MI. (C&D) Time curves for EF and FS, as indicators for heart function (n = 8 for lyoPV, n = 7 for lyoPV + aCD8). (E) Characteristic heart images on Day 28 post-MI, with infarct area indicated by blue lines. Scale bar, 2mm. (F) Quantification of heart weight to tibia length or body weight (n = 8 for lyoPV, n = 7 for lyoPV + aCD8). (G&H) Characteristic Masson trichrome staining on Day 28 post-MI and percentage of infarct area (n = 8 for lyoPV, n = 7 for

lyoPV + aCD8). Scale bar, 2 mm. Values were expressed as mean ± SEM and calculated via unpaired Student's *t*-test, one-way or two-way ANOVA with Tukey correction, as appropriate. ***: $P < 0.001$, **: $P < 0.01$, *: $P < 0.05$, *ns*: not significant.

Biosafety, organ distribution, and pharmacokinetics of PD-L1@NV *in vivo*

To rigorously assess the biosafety of lyophilized PD-L1@NV for *in vivo* application, a comprehensive study was conducted on Day 28 post-MI following indicated interventions (Figure 9A). Notably, Hematoxylin and Eosin (H&E) staining of critical organs, including the brain, spleen, kidney, lung, and liver, revealed no significant alterations in tissue structure, cellular morphology, or immune cell infiltration in both groups (Figure 9B). Additionally, assessments of hepatic and renal toxicities post-injection indicated that serum levels of alanine transaminase, aspartate transaminase, blood urea nitrogen, and creatinine remained stable (Figure 9C&D). In addition, PD-L1@NV exhibited minimal hemolysis at increasing concentrations, with a ratio well below the acceptable 5% threshold (Figure 9E&F).

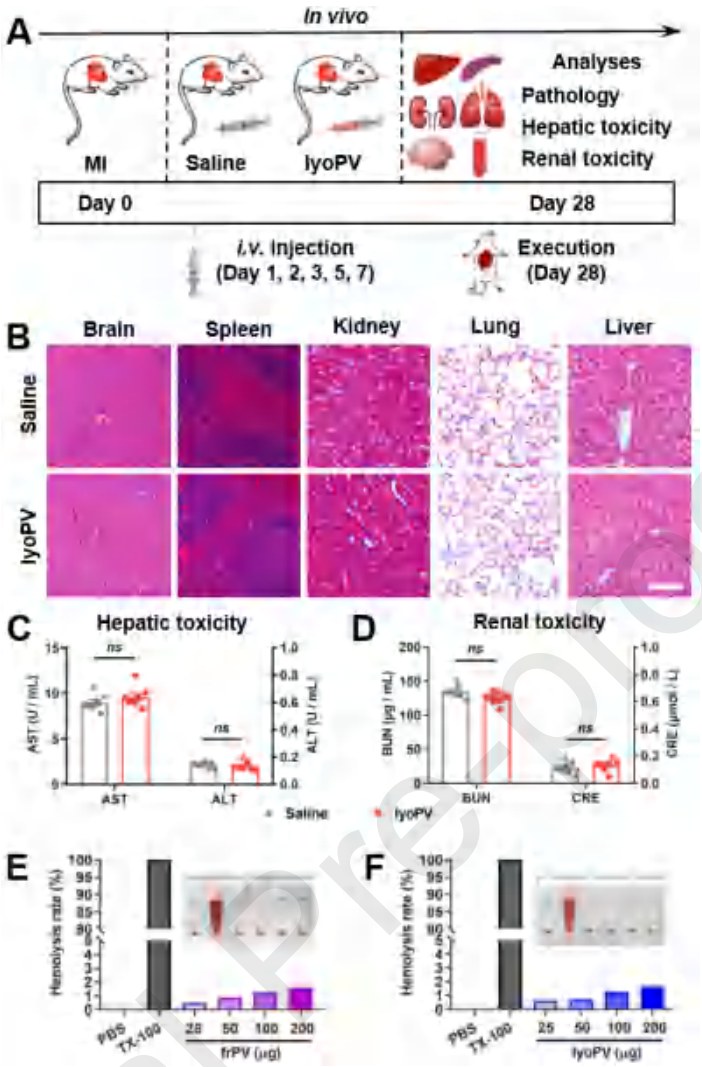

Figure 9. Safety evaluation of PD-L1@NV. (A) Experimental protocol for safety evaluation of engineered PD-L1@NV. (B) Histological examination of H&E-stained paraffin-embedded tissue sections. Scale bar, 100 μm. (C&D) Serum indices for hepatic and renal toxicity (n = 8). (E&F) Immunogenicity of fresh and lyophilized PD-L1@NV detected via hemolysis assay (n = 4). AST, aspartate aminotransferase; ALT, alanine aminotransferase; BUN, blood urea nitrogen; CRE, creatinine. Values were expressed as mean ± SEM and calculated via unpaired Student's t-test, one-way or two-way ANOVA with Tukey correction, as appropriate. *ns*: not significant.

Finally, organ distribution and pharmacokinetics of DiR-labeled PD-L1@NV were investigated in MI mice. Notably, the liver was identified as the primary site for drug accumulation (Figure 10A&B), exhibiting a time-dependent decline in signal intensity (Figure 10C). In contrast, fluorescence intensity in other organs remained relatively stable (Figure 10C). Collectively, these findings substantiate the biocompatibility, biodistribution, and pharmacokinetics of lyophilized PD-L1@NV, thereby confirming its safety and potential for future therapeutic applications.

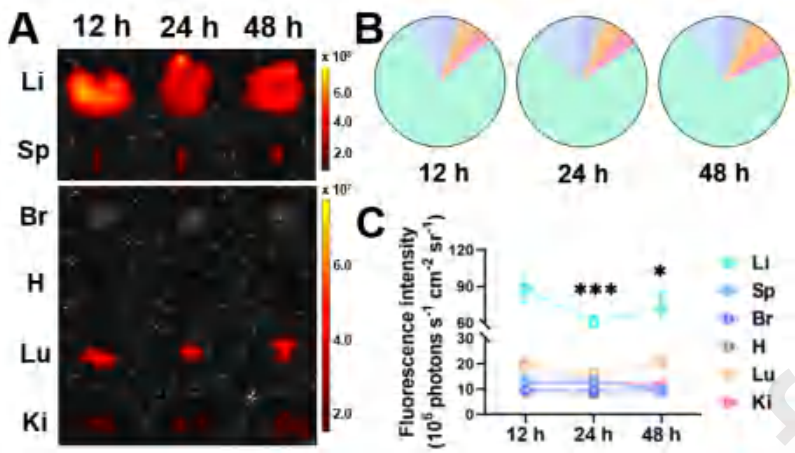

Figure 10. Organ distribution and pharmacokinetics of PD-L1@NV. DiR-labeled lyophilized PD-L1@NV was injected into MI mice via the tail vein. (A&B) *Ex vivo* optical imaging and pie charts for organ distribution were shown. (C) Time curves for drug pharmacokinetics (n = 5). */*** for comparison with 12 h. Li, liver; Sp, spleen; Br, brain; H, heart; Lu, lung; Ki, kidney. Values were expressed as mean ± SEM and calculated via two-way ANOVA with Tukey correction, as appropriate. ***: $P < 0.001$, *: $P < 0.05$.

Conclusion

We have developed a lentivirus-based, room-temperature-stable PD-L1@NV immunosuppressive nanovesicle, featuring membranous PD-L1, through serial extrusion and lyophilization. This vesicle has demonstrated considerable promise in mitigating MI-associated immunopathology, which in turn promotes aids in myocardial ischemic repair. Further mechanistic investigations revealed that PD-L1@NV effectively suppresses T cell activation in vitro and modulates T cell dynamics in vivo, primarily by disrupting the PD-1/PD-L1 interaction. Distinguished from traditional conjugation-based chemical methods or small extracellular vesicle-based biological therapies, our membrane-derived vesicles stand out due to simplicity, scalability, stability, and safety. These characteristics substantially enhance their commercial viability and establish PD-L1@NV as a promising candidate for clinical applications.

Acknowledgments

This work was partially supported by the National Natural Science Foundation of China (82070363 and 92168203), National Key R&D Program of China (2022YFA1104300), Jiangsu Cardiovascular Medicine Innovation Center (CXZX202210), Taishan Scholar Project of Shandong Province of China (tstp20240852), Scientific Research Project of Jiangsu Commission of Health (M2022010), Medical Innovation Application Research Project of Suzhou Science and Technology Bureau (SKY2022131), Boxi Youth Natural Science Foundation (BXQN2023016), and Priority Academic Program Development of Jiangsu Higher Education Institutions. The authors would also like to acknowledge several H&E staining services provided by zkec (www.zkec.cc).

Author contributions

Conceptualization, WC, WZ, QT; Investigation, QT, ML, SW, JL, SC, HL, YW; Methodology, SW, JL, HL, YC, HS, WZ; Formal analysis, QT, ML; Data curation, QT; Validation, QT, ML, SW; Writing-original draft, QT; Writing-review & editing, WC, WZ; Supervision, WC; Project administration, ZS, WC; Funding acquisition, WC, ZS, HS, YC.

Conflict of interests

There are no conflicts of interest to declare.

Data availability statement

The raw sequencing data are available in the Genome Sequence Archive at the BIG Data Center, Beijing Institute of Genomics (BIG), Chinese Academy of Sciences (https://bigd.big.ac.cn/), under accession number CRA016478

Reference

1. Bhatt DL, Lopes RD, Harrington RA: **Diagnosis and treatment of acute coronary syndromes: a review**. *JAMA* 2022, **327**(7):662-675.

2. Frangogiannis NG: **The inflammatory response in myocardial injury, repair, and remodelling**. *Nat Rev Cardiol* 2014, **11**(5):255-265.

3. Adamo L, Rocha-Resende C, Prabhu SD, Mann DL: **Reappraising the role of inflammation in heart failure**. *Nat Rev Cardiol* 2020, **17**(5):269-285.

4. Martini E, Kunderfranco P, Peano C, Carullo P, Cremonesi M, Schorn T, Carriero R, Termanini A, Colombo FS, Jachetti E *et al*: **Single-Cell Sequencing of Mouse Heart Immune Infiltrate in Pressure Overload-Driven Heart Failure Reveals Extent of Immune Activation**. *Circulation* 2019, **140**(25):2089-2107.

5. Calcagno DM, Taghdiri N, Ninh VK, Mesfin JM, Toomu A, Sehgal R, Lee J, Liang Y, Duran JM, Adler E *et al*: **Single-cell and spatial transcriptomics of the infarcted heart define the dynamic onset of the border zone in response to mechanical destabilization**. *Nat Cardiovasc Res* 2022, **1**(11):1039-1055.

6. Santos-Zas I, Lemarié J, Zlatanova I, Cachanado M, Seghezzi JC, Benamer H, Goube P, Vandestienne M, Cohen R, Ezzo M *et al*: **Cytotoxic CD8(+) T cells promote granzyme B-dependent adverse post-ischemic cardiac remodeling**. *Nat Commun* 2021, **12**(1):1483.

7. Ben Nasr M, Tezza S, D'Addio F, Mameli C, Usuelli V, Maestroni A, Corradi D, Belletti S, Albarello L, Becchi G *et al*: **PD-L1 genetic overexpression or pharmacological restoration in hematopoietic stem and progenitor cells reverses autoimmune diabetes**. *Sci Transl Med* 2017, **9**(416):eaam7543.

8. Wang L, Qi C, Cao H, Zhang Y, Liu X, Qiu L, Wang H, Xu L, Wu Z, Liu J *et al*: **Engineered cytokine-**

primed extracellular vesicles with high PD-L1 expression ameliorate Type 1 diabetes. *Small* 2023, **19**(38):e2301019.

9. Yang Z, Zhang Z, Li L, Jing Z, Ma Y, Lan T, Li Y, Lin Z, Fang W, Zhang J *et al*: **Bioengineered Artificial Extracellular Vesicles Presenting PD-L1 and Gal-9 Ameliorate New-Onset Type 1 Diabetes**. *Diabetes* 2024, **73**(8):1325-1335.

10. Han L, Zhen G, Jiacan S: **Engineered mammalian and bacterial extracellular vesicles as promising nanocarriers for targeted therapy**. *Extracell Vesicles Circ Nucleic Acids* 2022, **3**(2):63-86.

11. Han C, Yang J, Sun J, Qin G: **Extracellular vesicles in cardiovascular disease: Biological functions and therapeutic implications**. *Pharmacol Ther* 2022, **233**:108025.

12. Rao L, Wu L, Liu Z, Tian R, Yu G, Zhou Z, Yang K, Xiong HG, Zhang A, Yu GT *et al*: **Hybrid cellular membrane nanovesicles amplify macrophage immune responses against cancer recurrence and metastasis**. *Nat Commun* 2020, **11**(1):4909.

13. Fonte P, Reis S, Sarmento B: **Facts and evidences on the lyophilization of polymeric nanoparticles for drug delivery**. *J Control Release* 2016, **225**:75-86.

14. Augello A, Tasso R, Negrini SM, Amateis A, Indiveri F, Cancedda R, Pennesi G: **Bone marrow mesenchymal progenitor cells inhibit lymphocyte proliferation by activation of the programmed death 1 pathway**. *Eur J Immunol* 2005, **35**(5):1482-1490.

15. Li L, Zhang Y, Mu J, Chen J, Zhang C, Cao H, Gao J: **Transplantation of human mesenchymal stem-cell-derived exosomes immobilized in an adhesive hydrogel for effective treatment of spinal cord injury**. *Nano Lett* 2020, **20**(6):4298-4305.

16. Xiao W, Chen M, Zhou W, Ding L, Yang Z, Shao L, Li J, Chen W, Shen Z: **An immunometabolic patch facilitates mesenchymal stromal/stem cell therapy for myocardial infarction through a macrophage-dependent mechanism**. *Bioeng Transl Med* 2023, **8**(3):e10471.

17. Xie J, Hu Y, Li H, Wang Y, Fan X, Lu W, Liao R, Wang H, Cheng Y, Yang Y *et al*: **Targeted therapy for peri-prosthetic osteolysis using macrophage membrane-encapsulated human urine-derived stem cell extracellular vesicles**. *Acta Biomater* 2023, **160**:297-310.

18. Popowski KD, Moatti A, Scull G, Silkstone D, Lutz H, López de Juan Abad B, George A, Belcher E, Zhu D, Mei X *et al*: **Inhalable dry powder mRNA vaccines based on extracellular vesicles**. *Matter* 2022, **5**(9):2960-2974.

19. Ye Z, Zhang T, He W, Jin H, Liu C, Yang Z, Ren J: **Methotrexate-loaded extracellular vesicles functionalized with therapeutic and targeted peptides for the treatment of glioblastoma multiforme**. *ACS Appl Mater Interfaces* 2018, **10**(15):12341-12350.

20. Zhang J, Fu B, Li M, Mi S: **Secretome of activated fibroblasts induced by exosomes for the discovery of biomarkers in non-small cell lung cancer**. *Small* 2021, **17**(4):e2004750.

21. Yang H, Xiong Z, Heng X, Niu X, Wang Y, Yao L, Sun L, Liu Z, Chen H: **Click-chemistry-mediated cell membrane glycopolymer engineering to potentiate dendritic cell vaccines**. *Angew Chem Int Ed Engl* 2024, **63**(2):e202315782.

22. Yang Y, Zhang J, Wu S, Deng Y, Wang S, Xie L, Li X, Yang L: **Exosome/antimicrobial peptide laden hydrogel wound dressings promote scarless wound healing through miR-21-5p-mediated multiple functions**. *Biomaterials* 2024, **308**:122558.

23. Yang W, Pang Y, Wang X, Lai Z, Lu Y, Zheng S, Wang W: **A novel CTLA-4 blocking strategy based on nanobody enhances the activity of dendritic cell vaccine-stimulated antitumor cytotoxic T lymphocytes**. *Cell Death Dis* 2023, **14**(7):406.

24. Hao Y, Stuart T, Kowalski MH, Choudhary S, Hoffman P, Hartman A, Srivastava A, Molla G, Madad S, Fernandez-Granda C *et al*: **Dictionary learning for integrative, multimodal and scalable single-cell analysis**. *Nat Biotechnol* 2024, **42**(2):293-304.

25. Franzén O, Gan LM, Björkegren JLM: **PanglaoDB: a web server for exploration of mouse and human single-cell RNA sequencing data**. *Database (Oxford)* 2019, **2019**:baz046.

26. Zhou Y, Zhou B, Pache L, Chang M, Khodabakhshi AH, Tanaseichuk O, Benner C, Chanda SK: **Metascape provides a biologist-oriented resource for the analysis of systems-level datasets**. *Nat Commun* 2019, **10**(1):1523.

27. Wu T, Hu E, Xu S, Chen M, Guo P, Dai Z, Feng T, Zhou L, Tang W, Zhan L *et al*: **clusterProfiler 4.0: A universal enrichment tool for interpreting omics data**. *Innovation (Camb)* 2021, **2**(3):100141.

28. Chen X, Zhu S, Li HD, Wang JN, Sun LJ, Xu JJ, Hui YR, Li XF, Li LY, Zhao YX *et al*: **N(6)-methyladenosine-modified circIRF2, identified by YTHDF2, suppresses liver fibrosis via facilitating FOXO3 nuclear translocation**. *Int J Biol Macromol* 2023, **248**:125811.

29. Zhang R, Su K, Yang L, Tang M, Zhao M, Ye N, Cai X, Jiang X, Li N, Peng J *et al*: **Design, Synthesis, and Biological Evaluation of Novel P2X7 Receptor Antagonists for the Treatment of Septic Acute Kidney Injury**. *J Med Chem* 2023, **66**(16):11365-11389.

30. Wu W, Guo H, Jing D, Zhang Z, Zhang Z, Pu F, Yang W, Jin X, Huang X, Shao Z: **Targeted delivery of PD-L1-derived phosphorylation-mimicking peptides by engineered biomimetic nanovesicles to enhance osteosarcoma treatment**. *Adv Healthc Mater* 2022, **11**(23):e2200955.

31. Liu X, Jiang J, Chan R, Ji Y, Lu J, Liao YP, Okene M, Lin J, Lin P, Chang CH *et al*: **Improved efficacy and reduced toxicity using a custom-designed irinotecan-delivering silicasome for orthotopic colon cancer**. *ACS Nano* 2019, **13**(1):38-53.

32. Han C, Yang J, Zhang E, Jiang Y, Qiao A, Du Y, Zhang Q, An J, Sun J, Wang M *et al*: **Metabolic labeling of cardiomyocyte-derived small extracellular-vesicle (sEV) miRNAs identifies miR-208a in cardiac regulation of lung gene expression**. *J Extracell Vesicles* 2022, **11**(10):e12246.

33. Li Q, Xu Y, Lv K, Wang Y, Zhong Z, Xiao C, Zhu K, Ni C, Wang K, Kong M *et al*: **Small extracellular vesicles containing miR-486-5p promote angiogenesis after myocardial infarction in mice and nonhuman primates**. *Sci Transl Med* 2021, **13**(584):eabb0202.

34. Bei Y, Zhu Y, Wei M, Yin M, Li L, Chen C, Huang Z, Liang X, Gao J, Yao J *et al*: **HIPK1 inhibition protects against pathological cardiac hypertrophy by inhibiting the CREB-C/EBPβ axis**. *Adv Sci (Weinh)* 2023, **10**(18):e2300585.

35. Sun X, Chen H, Gao R, Qu Y, Huang Y, Zhang N, Hu S, Fan F, Zou Y, Hu K *et al*: **Intravenous transplantation of an ischemic-specific peptide-TPP-mitochondrial compound alleviates myocardial ischemic reperfusion injury**. *ACS Nano* 2023, **17**(2):896-909.

36. Zhou W, Jiang X, Tang Q, Ding L, Xiao W, Li J, Wu Y, Ruan HB, Shen Z, Chen W: **Glucosamine facilitates cardiac ischemic recovery via recruiting Ly6C(low) monocytes in a STAT1 and O-GlcNAcylation-dependent fashion**. *Clin Transl Med* 2022, **12**(3):e762.

37. Ding L, Zhou W, Zhang J, Tang Q, Xiao W, Chen M, Shen Z, Chen W: **Calming egress of inflammatory monocytes and related septic shock by therapeutic CCR2 silencing using macrophage-derived extracellular vesicles**. *Nanoscale* 2022, **14**(13):4935-4945.

38. Ma Q, Fan Q, Han X, Dong Z, Xu J, Bai J, Tao W, Sun D, Wang C: **Platelet-derived extracellular vesicles to target plaque inflammation for effective anti-atherosclerotic therapy**. *J Control Release* 2021, **329**:445-453.

39. Chen W, Gu P, Jiang X, Ruan HB, Li C, Gao X: **Protein phosphatase 2A catalytic subunit α (PP2Acα) maintains survival of committed erythroid cells in fetal liver erythropoiesis through the STAT5 pathway**. *Am J Pathol* 2011, **178**(5):2333-2343.

40. Zhou W, Tang Q, Wang S, Ding L, Chen M, Liu H, Wu Y, Xiong X, Shen Z, Chen W: **Local thiamet-G delivery by a thermosensitive hydrogel confers ischemic cardiac repair via myeloid M2-like activation in a STAT6 O-GlcNAcylation-dependent manner**. *Int Immunopharmacol* 2024, **131**:111883.

41. Wang B, Wu C, He S, Wang Y, Wang D, Tao H, Wang C, Pang X, Li F, Yuan Y *et al*: **V1-Cal hydrogelation enhances its effects on ventricular remodeling reduction and cardiac function improvement post myocardial infarction**. *Chem Eng J* 2022, **433**(Pt 1):134450.

42. Zhao P, Zhou W, Zhang Y, Li J, Zhao Y, Pan L, Shen Z, Chen W, Hui J: **Aminooxyacetic acid attenuates post-infarct cardiac dysfunction by balancing macrophage polarization through modulating macrophage metabolism in mice**. *J Cell Mol Med* 2020, **24**(4):2593-2609.

43. Xu F, Fei Z, Dai H, Xu J, Fan Q, Shen S, Zhang Y, Ma Q, Chu J, Peng F *et al*: **Mesenchymal stem cell-derived extracellular vesicles with high PD-L1 expression for autoimmune diseases treatment**. *Adv Mater* 2022, **34**(1):e2106265.

44. Sheng C, Guo X, Wan Z, Bai X, Liu H, Zhang X, Zhang P, Liu Y, Li W, Zhou Y *et al*: **Exosomes derived from human adipose-derived stem cells ameliorate osteoporosis through miR-335-**

3p/Aplnr axis. *Nano Res* 2022, **15**(10):9135-9148.

45. Wang C, Li N, Li Y, Hou S, Zhang W, Meng Z, Wang S, Jia Q, Tan J, Wang R *et al*: **Engineering a HEK-293T exosome-based delivery platform for efficient tumor-targeting chemotherapy/internal irradiation combination therapy**. *J Nanobiotechnology* 2022, **20**(1):247.

46. Chen M, Wang S, Chen Y, Shen H, Chen L, Ding L, Tang Q, Yang Z, Chen W, Shen Z: **Precision cardiac targeting: empowering curcumin therapy through smart exosome-mediated drug delivery in myocardial infarction**. *Regen Biomater* 2024, **11**:rbad108.

47. Zhao Y, Zhao X, Xu H, Xing Y, Wu T, Sun X, Kuang M, Ma X, Liu W, Yang Q: **Wharton's jelly MSC-derived extracellular vehicles—loaded hyaluronic acid-alginate adhesives for treatment of osteoarthritis**. *J Mater Sci Mater Med* 2023, **142**:240-252.

48. Yang K, Fan M, Wang X, Xu J, Wang Y, Tu F, Gill PS, Ha T, Liu L, Williams DL *et al*: **Lactate promotes macrophage HMGB1 lactylation, acetylation, and exosomal release in polymicrobial sepsis**. *Cell Death Differ* 2022, **29**(1):133-146.

49. Fang Z, Zhao G, Zhao S, Yu X, Feng R, Zhang YE, Li H, Huang L, Guo Z, Zhang Z *et al*: **GTF2H4 regulates partial EndMT via NF-κB activation through NCOA3 phosphorylation in ischemic diseases**. *Innovation (Camb)* 2024, **5**(2):100565.

50. Chen W, Xia J, Hu P, Zhou F, Chen Y, Wu J, Lei W, Shen Z: **Follistatin-like 1 protects cardiomyoblasts from injury induced by sodium nitroprusside through modulating Akt and Smad1/5/9 signaling**. *Biochem Biophys Res Commun* 2016, **469**(3):418-423.

51. Chen W, Wang S, Xia J, Huang Z, Tu X, Shen Z: **Protein phosphatase 2A plays an important role in migration of bone marrow stroma cells**. *Mol Cell Biochem* 2016, **412**(1-2):173-180.

52. Ma C, Li Y, Tian M, Deng Q, Qin X, Lu H, Gao J, Chen M, Weinstein LS, Zhang M *et al*: **Gsα regulates macrophage foam cell formation during atherosclerosis**. *Circ Res* 2024, **134**(7):e34-e51.

53. Zhang Q, Esplin BL, Iida R, Garrett KP, Huang ZL, Medina KL, Kincade PW: **RAG-1 and Ly6D independently reflect progression in the B lymphoid lineage**. *PLoS One* 2013, **8**(8):e72397.

54. Liu Z, Zhang H, Xia H, Wang B, Zhang R, Zeng Q, Guo L, Shen K, Wang B, Zhong Y *et al*: **CD8 T cell-derived perforin aggravates secondary spinal cord injury through destroying the blood-spinal cord barrier**. *Biochem Biophys Res Commun* 2019, **512**(2):367-372.

55. Emmert-Streib F, Glazko GV: **Pathway analysis of expression data: deciphering functional building blocks of complex diseases**. *PLoS Comput Biol* 2011, **7**(5):e1002053.

56. Ilatovskaya DV, Pitts C, Clayton J, Domondon M, Troncoso M, Pippin S, DeLeon-Pennell KY: **CD8(+) T-cells negatively regulate inflammation post-myocardial infarction**. *Am J Physiol Heart Circ Physiol* 2019, **317**(3):H581-h596.

57. Weirather J, Hofmann UD, Beyersdorf N, Ramos GC, Vogel B, Frey A, Ertl G, Kerkau T, Frantz S: **Foxp3+ CD4+ T cells improve healing after myocardial infarction by modulating monocyte/macrophage differentiation**. *Circ Res* 2014, **115**(1):55-67.

Highlights

- Membrane extrusion is more cost-effective than secrotome-based extracellular vesicles.
- Lyophilized nanovesicles surpass their liquid formulations in stability.
- PD-L1@NV effectively suppresses proliferation and activation of CD8 T lymphocytes.
- PD-L1@NV therapy facilitates myocardial recovery via the PD-1/PD-L1 axis.
- PD-L1@NV reshapes T-cell dynamics *in vivo*, counteracting ischemic immunopathology.